Micro-Computed Tomography Beamline of the Australian Synchrotron: Micron-Size Spatial Resolution X-ray Imaging

Benedicta D. Arhatari [1,*], Andrew W. Stevenson [1,2], Darren Thompson [1,2], Adam Walsh [1], Tom Fiala [1], Gary Ruben [1], Nader Afshar [1], Sinem Ozbilgen [1], Tingting Feng [1], Stephen Mudie [1] and Prithi Tissa [1]

1 Australian Synchrotron, Australian Nuclear Science and Technology Organisation (ANSTO), Clayton, VIC 3168, Australia
2 Commonwealth Scientific and Industrial Research Organisation (CSIRO), Clayton, VIC 3168, Australia
* Correspondence: arhatarb@ansto.gov.au

Abstract: The first new beamline of the BRIGHT project—involving the construction of eight new beamlines at the Australian Synchrotron—is the Micro-Computed Tomography (MCT) beamline. MCT will extend the facility's capability for higher spatial resolution X-ray-computed tomographic imaging allowing for commensurately smaller samples in comparison with the existing Imaging and Medical Beamline (IMBL). The source is a bending-magnet and it is operating in the X-ray energy range from 8 to 40 keV. The beamline provides important new capability for a range of biological and material-science applications. Several imaging modes will be offered such as various X-ray phase-contrast modalities (propagation-based, grating-based, and speckle-based), in addition to conventional absorption contrast. The unique properties of synchrotron radiation sources (high coherence, energy tunability, and high brightness) are predominantly well-suited for producing phase contrast data. An update on the progress of the MCT project in delivering high-spatial-resolution imaging (in the order of micron size) of mm-scale objects will be presented in detail with some imaging results from the hot-commissioning stage.

Keywords: X-ray micro-CT; absorption contrast; phase-contrast; computed tomography; synchrotron

1. Introduction

The Micro-Computed Tomography (MCT) Beamline is a 1.3 T bending-magnet-based beamline at the third generation 3 GeV (200 mA) Australian Synchrotron that is operated by the Australian Nuclear Science and Technology Organisation (ANSTO). It is the first of the eight new beamlines being constructed as part of the BRIGHT project and can produce nearly parallel polychromatic and monochromatic X-ray beams with energies ranging from 8 to 40 keV through the use of a double multilayer monochromator (DMM). The MCT user experimental program will encompass widespread applications from material to life sciences. In most cases, the experiments are performed under ambient conditions. However, for some material-science applications in the near future, the beamline will incorporate specialized sample stages for heating, cooling, or performing in-liquid experiments. In situ loading during measurements can also be subjected to the sample, including tensile stress, compression, etc. Several imaging modalities are offered at MCT for both 2D and/or 3D imaging, including propagation-based phase-contrast techniques [1–4] at the current stage of development and, in the future, grating-based techniques [5,6], speckle-based techniques [7–9], dark field imaging [10], and nano-CT imaging [11]. The choice of technique depends mainly on the specific application and science drivers. Dynamic or high-speed imaging (as a function of time) [12–14] will also be available due to the comparatively high X-ray flux at MCT relative to laboratory-based sources.

There are three hutches at the MCT beamline. Hutch A is the beam-conditioning hutch and houses the photon delivery system (PDS), including key X-ray optical elements.

The experiment hutches are B and C, in order of increasing distance from the source, with a maximum distance of over 34 m from the source at the end of hutch C. There is a removable beam stop at the end of hutch B. This allows access to hutch C while an experiment is being conducted inside hutch B. The beam size in the sample plane inside Hutch B (22 m from the source) is 44 mm (horizontally) × 6.6 mm (vertically), as defined by the mask in the PDS. In hutch C (32 m from the source), the beam size is 64 mm (horizontally) × 9.6 mm (vertically).

The PDS in hutch A will deliver nearly parallel X-rays. Four different beam modes will be available, i.e., white beam, pink beam, and monochromatic beam with and without harmonic suppression. A schematic spectrum of the four-beam modes is shown in Figure 1. The white beam (as shown in Figure 1a) is a polychromatic unfiltered beam directly from the first bending magnet source in sector 9 of the Australian Synchrotron storage ring. The pink beam (as shown in Figure 1b) is achieved by cutting off the high energy end of the white beam using a Vertical Bounce Mirror (VBM). A double-multilayer monochromator (DMM) is used to produce a monochromatic beam with the energy bandpass of 0.5% or 3% depending on the DMM stripe used. A monochromatic beam is schematically shown in Figure 1c with the presence of a small contribution from the third harmonic. The small, undesired third harmonic component from the monochromatic beam can be removed by using the VBM if necessary, as shown in Figure 1d.
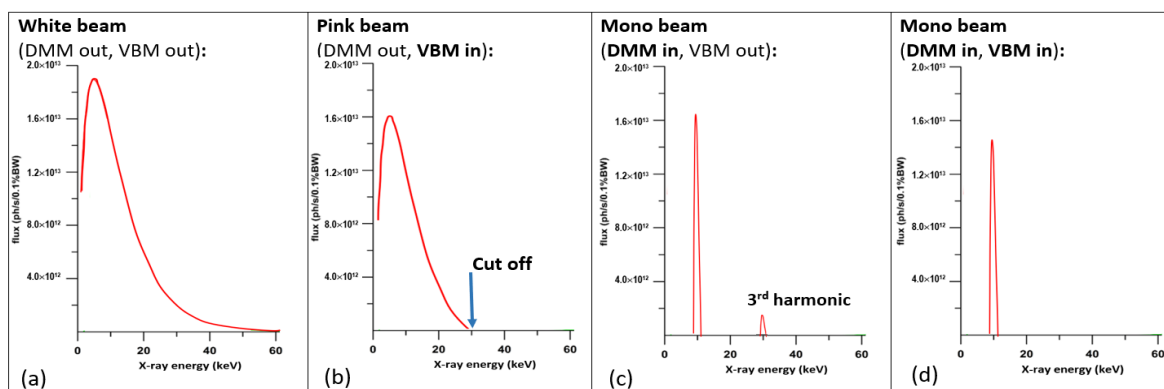
Figure 1. Four different beam modes in MCT beamline: (**a**) white beam, (**b**) pink beam, (**c**) monochromatic beam, and (**d**) monochromatic beam without a third harmonic contribution.

The beamline layout for MCT is shown in Figure 2. There are four vacuum sections in PDS (in Hutch A). PDS vacuum section #1 consists of mask, white beam slit A, and filters with five paddles. These filters are useful to harden the beam or remove the low energy parts. The DMM is in PDS vacuum section #2. The substrate material of the DMM is single-crystal silicon. There are three stripes in the DMM with the coating material of Ru/C (for 8–23 keV, 3% bandpass), V/B_4C (for 8–25 keV, 0.5% bandpass), and W/B_4C (21–40 keV, 3% bandpass). The first multilayer of the DMM is at a fixed location of 13 m from the source while the second multilayer can be moved up-stream/down-stream during the operation. The X-ray energy of the beam will be defined by the pitch position of both multilayers. In practice, the energy calibration must be performed during the hot commissioning stage in order to achieve the true X-ray energy for user operation. PDS vacuum section #3 consists of a diagnostic screen, white beam slit B, and VBM. The substrate material of the VBM is also single-crystal silicon. There are two stripes in the VBM with the coating material of Rh and Pt. The choice of the stripe and the pitch position of the VBM will define the cut off X-ray energy at the high-energy end. Lastly, PDS vacuum section #4 consists of another diagnostic screen, white beam slit C, photon shutter, and safety shutter.
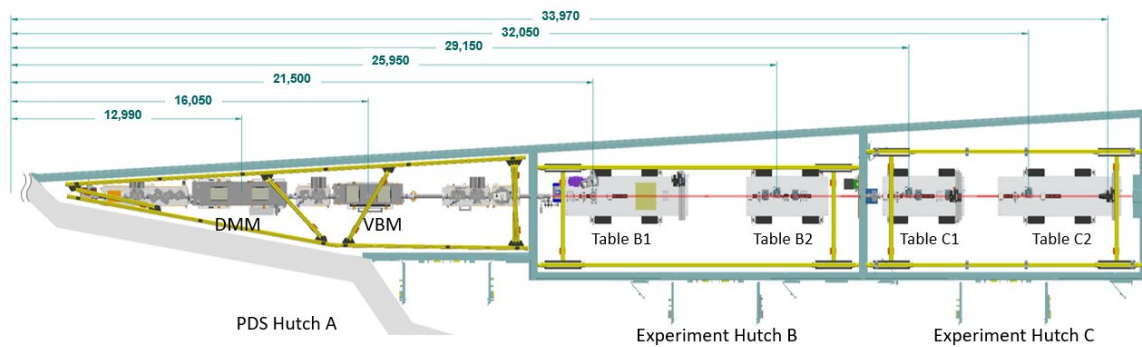
Figure 2. MCT beamline layout.

There are two granite tables each in experiment hutch B and C, respectively. The first table (Table B1) in experiment hutch B is the work horse table for absorption-contrast and propagation-based phase-contrast imaging. The sample stage and detector stage is mounted in Table B1 in the early stage of user operation with movable sample-to-detector distance. A robot for rapid sample exchange is also mounted in this table. In future operation, the detector stage can be moved to other tables for other imaging modality. Table B2 (the second table in hutch B) will be used for a nano CT-based system with the detector in Table C2. The grating-based system and speckle-based system will be mounted in Table C1.

The MCT beamline has been designed in response to the needs of the user community (including industry) for high-resolution imaging applications and characterization of materials. This will provide enormous benefit to many 3D X-ray imaging applications [15–17] such as industrial inspection, medicine, material science, chemistry, and biomedical imaging. There will be two imaging modalities offered by the MCT beamline in the early stages of its operation. These are absorption-contrast and phase-contrast modes. In the phase-contrast mode, we will use a propagation-based phase-contrast imaging set-up. Propagation-based phase-contrast imaging has a simple experimental set-up that does not require any additional optical elements. This method merely allows a spatially coherent wave field to propagate far enough distance from the sample so that the diffraction fringes can be detected by the detector. Due to its simplicity, this propagation-based phase-contrast modality is readily applied to 3D computed tomography (CT) imaging [18–20]. Meanwhile, the absorption-contrast mode is attained when the sample-to-detector distance is very small. In this way, the phase-contrast is easily achieved by moving the detector away from the sample. The interaction between the X-ray beam and the sample can be generally described by the complex refractive index, $n = 1 - \delta + i\beta$, where δ is related to the phase shift and β is related to the attenuation. The contrast in conventional X-ray projection images primarily depends on the linear attenuation coefficient, $\mu(\lambda) = 4\pi\beta(\lambda)/\lambda$, where λ is the X-ray wavelength. The X-rays traverse point r as a specific location in an object, travel along a straight line $L(x,\theta)$, indicated by the path length, t, and are distinctively defined by the rotation angle, θ, and the end-point, x, at the projection (detector) plane. Hence, $\mu(r, \lambda)$ can be written as $\mu(r, \lambda) = \mu(x,\theta,t,\lambda)$. The output intensity, I, in the single wavelength case is provided by integrating the attenuation through the sample, as follows:

$$I(x,\theta,\lambda) = I_0.e^{-\int_{L(x,\theta)} \mu(x,\theta,t,\lambda)dt} = I_0.e^{-(\mathcal{R}\mu)(x,\theta,\lambda)} \tag{1}$$

where I_0 is the incident intensity and $\mathcal{R}$ is the Radon transform [21]. The linear attenuation coefficient on CT reconstruction can then be calculated via an inverse Radon transform operation

$$\mu(r,\lambda) = -\mathcal{R}^{-1}\left[ln\left(\frac{I(x,\theta,\lambda)}{I_0}\right)\right] \tag{2}$$

The distribution of the linear attenuation coefficient in the single wavelength case can also be expressed in terms of β, the distribution of the imaginary component of the complex X-ray refractive index as $\beta(\boldsymbol{r}, \lambda) = -\frac{\lambda}{4\pi}\, \boldsymbol{\mathcal{R}}^{-1}\left[ln\left(\frac{I(x,\theta,\lambda)}{I_0}\right)\right]$. For low density or low Z materials, the X-ray attenuation generates low contrast [22]. By comparison, in the hard X-ray regime, the contribution of δ is typically three orders of magnitude greater than the contribution of β. This has led to utilizing the refraction in hard X-ray phase-contrast imaging becoming an increasingly widespread technique for the non-destructive imaging of low-density samples [3,23]. Therefore, to obtain the distribution of $\delta(\boldsymbol{r},\lambda)$ we use:

$$\delta(\boldsymbol{r}, \lambda) = -\boldsymbol{\mathcal{R}}^{-1}[\delta(\lambda). \, T(x, \theta)] \tag{3}$$

where $T(x, \theta)$ is the retrieved thickness for a projection angle, θ. For homogeneous samples, this can be calculated using the "TIE-Hom" algorithm (also known as Paganin's method), as follows [24]:

$$T(x, \theta) = -\ln\left[\mathbb{F}^{-1}\left(\frac{\lambda}{4\pi\beta + z\delta\lambda u^2}\mathbb{F}\left[\frac{I_z(x, \theta, \lambda)}{I_0}\right]\right)\right] \tag{4}$$

where u is the Fourier variable conjugate of x, $\mathbb{F}$ is the Fourier transform operator, $\mathbb{F}^{-1}$ is the inverse Fourier transform, and $I_z(x, \theta, \lambda)$ is the intensity at a propagation distance with a fixed value of z. The TIE-Hom algorithm is predominantly useful for imaging approximately homogeneous low-density samples. Equation (4) is implemented using the propagation-based phase-contrast method that is often more straightforward compared to other phase-sensitive X-ray-imaging techniques [4,25].

The emphasis of the current paper is on the early development and progress of micron size resolution imaging (of mm-scale objects) at the MCT beamline including both propagation-based phase-contrast and absorption-contrast imaging modalities. More detail on the image resolution will be presented in terms of the results obtained during hot commissioning. Other imaging modes such as grating-based, speckle-based, and nano-CT are still in the process of development at the MCT beamline.

2. Early Development in MCT Beamline

2.1. The First Light

A major milestone for the BRIGHT project was the achievement of "first light" at the MCT beamline on 21 November 2021. "First light" involves obtaining X-rays from the storage ring into the PDS for the first time (the beam is confined to Hutch A with closed beamline shutters). The system was started with a low ring current of 1 mA, which is possible only during machine-studies time in the facility, when the front end was opened for the first time (with the storage ring operational) and without any optical elements in the X-ray's path in the PDS. The first light is detected using a diagnostic screen (created with a copper block coated with Yttrium oxide) located in the PDS. This diagnostic screen was lowered into the beam path and emits visible light when exposed to X-rays. This visible light was captured by the visible light camera that viewed the diagnostic screen, see Figure 3. By carefully monitoring the condition of the vacuum levels, water flows, and temperatures, the low current of 1 mA was increased systematically. On the following day, 22 November 2021, the operation with an increasing current up to the full ring current of 200 mA (top up mode) was achieved. Further conditioning and testing of the PDS was performed in the remaining user-beam time in 2021.
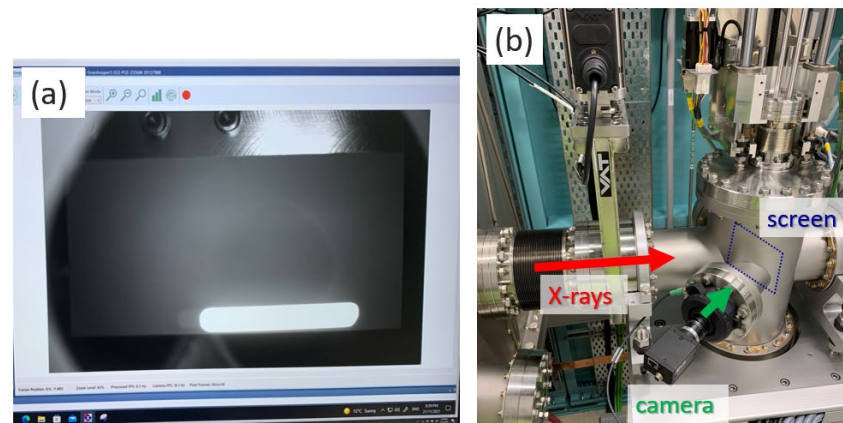
Figure 3. (**a**). Image of the "first light" captured by a visible light camera connected to a computer. (**b**). Diagnostic screen inside vacuum tube (blue dot line square) with visible light camera system (green arrow direction) that captured the X-rays (red arrow direction).

2.2. X-ray Detector

Due to different beam modes on the MCT beamline, in the early stage of its operation, we will have two different types of detectors, i.e., a white-beam detector and monochromatic-beam detector, see Figure 4. Each detector is supplied with several objective lenses that can be easily selected for each experiment to provide the required image magnification, field of view, and the corresponding resolution. Each detector is coupled with a high-resolution pco.edge 5.5 sCMOS camera that has 2560×2160 pixels and 6.5 μm $\times 6.5$ μm pixel size. The pco.edge camera is oriented perpendicular to the beam direction to prevent the direct beam impacting the camera. Each objective is coupled with thin LuAG:Ce or GGG:Eu/Tb scintillators that convert X-rays to visible light. This light goes to the objective lens and then to the pco.edge camera via a 45° mirror. In the white-beam detector, this 45° mirror is located between the scintillator and objective lens while in the monochromatic-beam detector between the objective lens and pco.edge camera. The white-beam detector is flushed with dry Nitrogen gas with a small flow of 0.15 lt/min during the experiment to prevent ozone degrading the mirror surface.
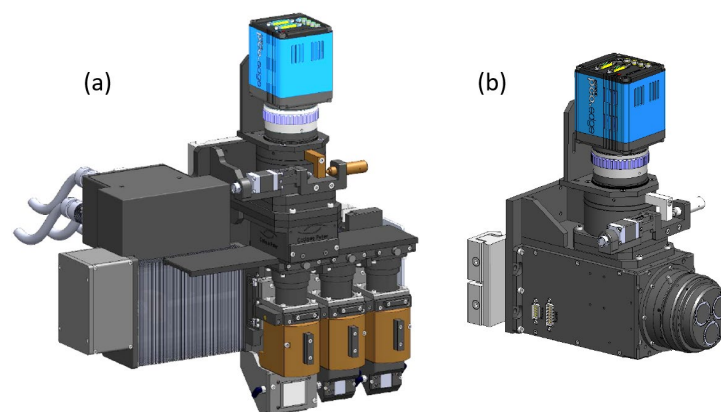
Figure 4. (**a**). White-beam detector with three objective lenses. (**b**). Monochromatic-beam detector with three objective lenses.

2.3. Spatial Resolution of the White-Beam Detector

The two imaging modalities offered by the MCT beamline in the early stage of its operation are absorption-contrast and propagation-based phase-contrast. The point spread function (PSF) of these imaging setups can be described as a combination of the blurring from the source size due to the geometric setup and the blurring from the detector itself.

The blurring from the source is due to the geometric magnification in the propagation-based imaging setup, whereas the blurring from the detector is mainly caused by the blurring associated with the scintillator thickness. A thin scintillator will contribute less to the PSF but then lowers the efficiency and so a compromise is needed. The standard deviation for the (normalized) Gaussian for the PSF for our imaging system can be presented as follows [2]:

$$\sigma_{sys} = \sqrt{\left(\frac{M-1}{M}\right)^2 \sigma_s^2 + \frac{\sigma_d^2}{M^2}} \tag{5}$$

where M is geometric magnification, σ_s is the Gaussian standard deviation for the source size, and σ_d is the standard deviation for the line spread function (LSF) of the detector, which, in this case, is mainly due to the scintillator blurring. The geometric magnification, M, is dependent on the distance between the source and the sample (R_1) and the sample and the detector (R_2) as $M = (R_1 + R_2)/R_1$. For the true absorption-contrast mode, where $R_2 = 0$ and $M = 1$, the first term of Equation (5) will be zero. This first term will become important when the sample to detector distance is large, $M > 1$. In the current set-up the source-sample distance R_1 is 21.5 m with the source size, σ_s, of 87 μm horizontally and 58 μm vertically. Koch et al. [26] use the expression for the Gaussian LSF at 90% and 50%. For non-Gaussian LSFs, we can describe σ_d as follows:

$$\sigma = \frac{\left(\sigma_{(fw90\%)} + \sigma_{(fw50\%)}\right)}{2}$$

$$\sigma \equiv \sigma_d = \sqrt{\left(\frac{0.19\,n\lambda_v}{NA}\right)^2 + (0.043\,s\,NA)^2} + \sqrt{\left(\frac{0.12\,n\lambda_v}{NA}\right)^2 + (0.028\,s\,NA)^2} \tag{6}$$

where $n = 1$ for the condition in air, NA is the numerical aperture, s is the scintillator thickness, and λ_v is the wavelength of visible light produced by the scintillator in response to the X-ray beam (550 nm in this case). For the MCT white-beam detector, we will have σ_d as shown in Table 1 as calculated using Equation (6). The information regarding the numerical aperture, scintillator thickness, FOV, and effective pixel size are also presented in Table 1. The white-beam detector uses LuAG:Ce scintillators with a different thickness for each objective lens of 1×, 5×, and 20×, respectively.

Table 1. The calculated detector standard deviation, σ_d, for MCT white-beam detector.

Objective Lens	NA	Scintillator Thickness (μm)	FOV (mm²)	Effective Pixel Size (μm)	σ_d (μm)
1×	0.035	500	16.6 × 14.0	6.5	5.03
5×	0.21	35	3.3 × 2.8	1.3	0.97
20×	0.42	10	0.8 × 0.7	0.33	0.50

The corresponding system standard deviation, σ_{sys}, for several sample-to-detector distances of 160 mm, 700 mm, and 1410 mm can be found in Table 2, as calculated using Equation (5), for the horizontal direction. The horizontal source blurring was calculated using the horizontal source size of 87 μm. Similarly, the vertical source blurring (not presented in the table) can be calculated using the vertical source size of 58 μm. The corresponding full width at half maximum (FWHM) can be calculated as res$_{FWHM}$ = $2\sqrt{2\,ln\,2}\,\sigma_{sys} \approx 2.355\,\sigma_{sys}$.

Table 2. The calculated system standard deviation, σ_{sys}, and res_{FWHM} in horizontal direction of MCT white-beam detector.

Objective Lens	Sample Detector Distance (mm)	M	Horizontal Source Blurring (μm)	σ_{sys} (Horizontally) (μm)	res_{FWHM} (Horizontally) (μm)
1×	160	1.01	0.64	5.03	11.85
	700	1.03	2.7	5.59	13.16
	1410	1.07	5.4	7.14	16.81
5×	160	1.01	0.64	1.15	2.72
	700	1.03	2.7	2.90	6.82
	1410	1.07	5.4	5.43	12.79
20×	160	1.01	0.64	0.81	1.92
	700	1.03	2.7	2.79	6.56
	1410	1.07	5.4	5.38	12.66

In order to evaluate the PSF for our imaging system, we use a MicroCT Bar Pattern Phantom (QRM GmbH, Germany) and a resolution test pattern (Xradia X500-200-30, ZEISS, California, USA) with a known size of line width. The first one will be used for the 1× objective lens, while the second one for the 5× and 20× objective lenses as they have different ranges of feature sizes. The MicroCT Bar Pattern phantom is composed of a silicon chip with various line widths. The Xradia X500-200-30 consists of an electroplated gold pattern on a Si_3N_4 membrane and incorporates line patterns of different sizes. We use three different sample-to-detector distances for this study, i.e., 160 mm, 700 mm, and 1410 mm. These will vary the geometrical magnification value of M. The experiment is conducted using white beam mode with an in vacuo filter of 0.2 mm diamond, 5 mm Al, and 0.1 mm Cu in the beam path. The images are corrected with a flat-field image and dark current image to account for the non-uniformity of the imaging system. The flat-field images were conducted with the X-ray illumination on, but without a sample within the field-of-view (FOV). The dark-current images were conducted without X-rays. The imaging results for both resolution phantoms are shown in Figures 5 and 6 for horizontal and vertical orientations, respectively. The images have been cropped to highlight the important regions of the test patterns. The corresponding theoretical res_{FWHM} values as shown in Table 2 are also presented in Figure 5 for easy comparison between the theoretical value and the experimental result.

The results obtained for the resolution test patterns from Figures 5 and 6 show good agreement with the theoretical horizontal and vertical resolution values. For example, in Figure 5, for the 1× objective lens at 160 mm and 700 mm distances, we do not resolve the 10 μm linewidth in the experimental results. These are in good agreement with the theoretical values of 11.85 μm and 13.16 μm, respectively. Note that the FWHM values of each pattern are the same with the corresponding linewidths. In another word, the theoretical FWHM values can be compared with the experimental linewidth values. Similarly, the smallest line width visible at 160 mm using the 20× objective lens is slightly below 2 μm. This is in good agreement with the corresponding theoretical resolution FWHM value of 1.92 μm. One minor exception in Figure 6 for the 5× objective lens at 160 mm distance is where the experimental result shows a slightly bigger value than the theoretical vertical resolution of 2.47 μm.

objective lens	R_2 (mm)	res_{FWHM} (μm)	
1×	160	11.85	
	700	13.16	
	1410	16.81	
5×	160	2.72	
	700	6.82	
	1410	12.79	
20×	160	1.92	
	700	6.56	
	1410	12.66	
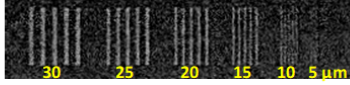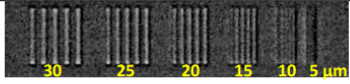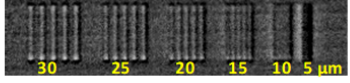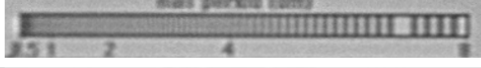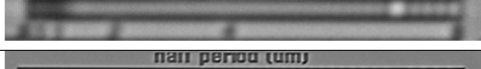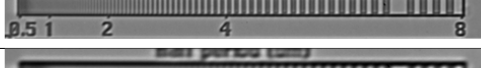
Figure 5. Resolution pattern images in horizontal direction taken using 1× objective lens (for QRM MicroCT test pattern) and using 5× and 20× objective lenses (for Xradia X500-200-30 test pattern) at several sample-to-detector distances of 160 mm, 700 mm, and 1410 mm with corresponding theoretical res_{FWHM} values horizontally. The numbers below the test pattern of 1× images indicate the corresponding linewidth in μm. The half period or linewidth in μm unit of the 5× and 20× objective lens images are visible on the pattern itself.

objective lens	1×			5×			20×		
R_2 (mm)	160	700	1410	160	700	1410	160	700	1410
res_{FWHM} (μm)	11.79	12.25	13.93	2.47	4.84	8.67	1.55	4.46	8.48
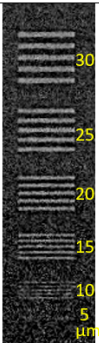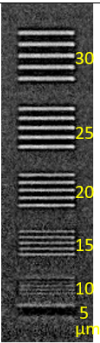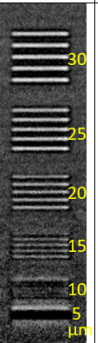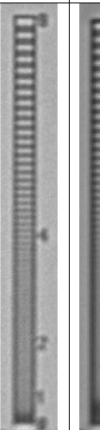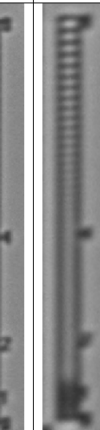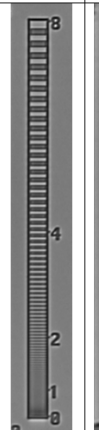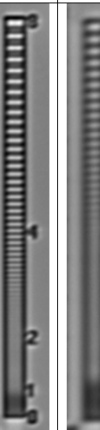
Figure 6. Resolution pattern images in vertical direction taken using 1× objective lens (for QRM MicroCT test pattern) and using 5× and 20× objective lenses (for Xradia X500-200-30 test pattern) at several sample-to-detector distances of 160 mm, 700 mm, and 1410 mm with corresponding theoretical resolution in res_{FWHM} values vertically.

3. Imaging Results from Hot Commissioning Stage

3.1. X-ray Phase Contrast Result

For data acquisition, the MCT beamline uses a web-browser-based user interface for common experiment types with continuous feedback and monitoring. The input values, such as file name, exposure time, beam mode, X-ray energy, number of projections, and number of darks and flats, can be entered via this user interface. There is also the option to choose 2D (projections) or 3D (tomographic) data acquisition. The produced data product is an hdf5 file, incorporating both image and metadata information.

The first phase-contrast images produced at the MCT beamline can be seen in Figure 7. A monochromatic beam at 11 keV was used to image an insect, fibrous paper, and eucalyptus leaf, using the 5× objective lens of the white-beam detector. The distance between the samples and detector was 70 mm. Phase contrast is clearly present in these images (manifesting itself as black-white fringes enhancing the edge structure of the sample in particular).
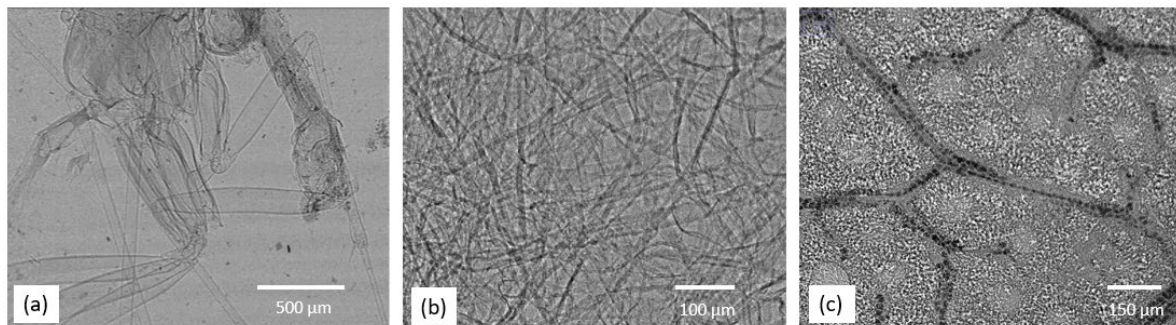
Figure 7. X-ray phase-contrast images (at 11 keV monochromatic beam collected using 5× objective lens): (**a**) an insect, (**b**) fibrous paper, and (**c**) a eucalyptus leaf.

3.2. X-ray Phase Contrast CT Result

For the tomographic scanning reported in this section, the sample is rotated over a 180° range. The data consisted of 1201 projections with a step-angle of 0.15°. Before and after the scan, 100 dark-current images and 100 flat-field images were collected.

Pre-processing each of the projection images is required prior to 3D reconstructions. This includes the correction for the dark-current and flat-field images. The pre-processing and the 3D reconstruction step were applied using the MCT processing pipeline and data processing user interface, developed by the Australian Synchrotron's in-house Scientific Computing group. The workflow and pipeline are configured and run from Jupyter notebooks. The pipeline is based on the open source Insight Toolkit (ITK) [27,28] and ASTRA toolbox [29] projects. The MCT processing pipeline was used for 3D reconstruction including the TIE-Hom phase-retrieval step. The phase-retrieval algorithm was applied to the projection data set, to exploit the information from the phase, using a γ (or the ratio δ/β) value applicable to the relevant materials at the experiment's X-ray energy. The Filtered Back Projection (FBP) algorithm [30] was used for the CT reconstruction. The MCT processing pipeline is available in the interactive computing environment ASCI (Australian Synchrotron Computer Infrastructure) desktop that provides high-performance computing resources [31]. The ASCI desktop provides a convenient web-based interface to launch Linux desktops on high-performance computer hardware. The experiment data are also stored in the ASCI desktop. The ASCI desktop can be used to analyze users' data immediately following acquisition at the beamline and/or after their beam time by logging in remotely. Analysis software such as ORS-Dragonfly and Avizo are also available in the ASCI desktop for MCT users. These software packages are useful for 3D viewing, image rendering, image segmentation to calculate volume, pore network analysis, bone analysis, etc.

Figure 8a,b show the reconstructed slices without and with phase-retrieval, respectively. We can see that the contrast is improved by TIE-Hom phase retrieval and shows an increased signal-to-noise ratio (SNR) [32,33] in Figure 8b compared to the one without phase retrieval (Figure 8a). The data were extracted using a white beam with in vacuo filtration of 0.2 mm diamond, 5 mm Al, and 0.1 mm Cu. The white beam detector was used with a $20\times$ objective lens with an exposure time of 0.7 s. The distance between the sample and detector was 160 mm. ORS-Dragonfly was then used for 3D representation.
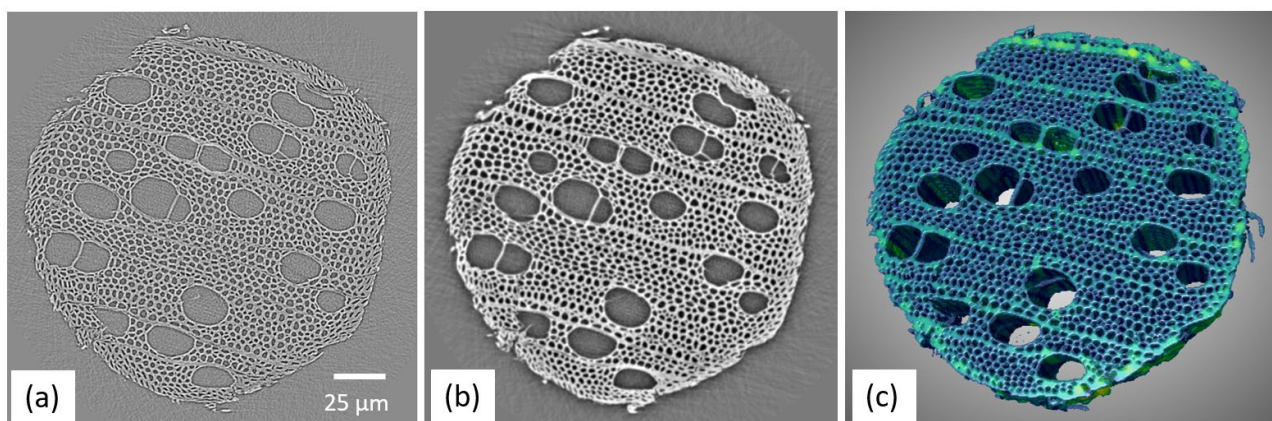
Figure 8. Slice reconstruction of wood structure (toothpick) without TIE-Hom phase-retrieval in (**a**) and with TIE-Hom phase-retrieval in (**b**), with the 3D visualization of the data such as in (**b**) presented in (**c**). Data were collected using white beam, $20\times$ objective lens, exposure time of 0.7 s, and sample-detector distance of 160 mm.

4. Conclusions

The MCT beamline constructed as part of the BRIGHT project at the ANSTO Australian Synchrotron is suitable for high-resolution computed tomographic imaging both in absorption-contrast and propagation-based phase-contrast imaging modalities. The resolution study for the white-beam detector showed good agreement between theoretical and experimental values. "First light", first phase-contrast images, and first CT data were produced successfully at the MCT beamline. The CT result showed that the phase-retrieval TIE-Hom algorithm can be used to enhance image contrast of low Z materials and improve SNR. The MCT users can rapidly process the collected data during their beam time and/or access the data after the beam time using the synchrotron's ASCI desktop facility. This new MCT beamline provides complementary capability to the IMBL beamline. This extends the capability of imaging for a broader range of object sizes and resolutions.

Author Contributions: All authors contributed equally to this work. All authors have read and agreed to the published version of the manuscript.

References

1. Gureyev, T.E.; Paganin, D.M.; Myers, G.R.; Nesterets, Y.I.; Wilkins, S.W. Phase-and-amplitude computer tomography. *Appl. Phys. Lett.* **2006**, *89*, 034102. [CrossRef]
2. Stevenson, A.W.; Hall, C.J.; Mayo, S.C.; Häusermann, D.; Maksimenko, A.; Gureyev, T.E.; Nesterets, Y.I.; Wilkins, S.W.; Lewis, R.A. Analysis and interpretation of the first monochromatic X-ray tomography data collected at the Australian Synchrotron Imaging and Medical beamline. *J. Synchrotron Radiat.* **2012**, *19*, 728–750. [CrossRef]
3. Snigirev, A.; Snigireva, I.; Kohn, V.; Kuznetsov, S.; Schelokov, I. On the possibilities of x-ray phase contrast microimaging by coherent high-energy synchrotron radiation. *Rev. Sci. Instrum.* **1995**, *66*, 5486–5492. [CrossRef]
4. Wilkins, S.W.; Gureyev, T.E.; Gao, D.; Pogany, A.; Stevenson, A.W. Phase-contrast imaging using polychromatic hard X-rays. *Nature* **1996**, *384*, 335–338. [CrossRef]
5. Morgan, K.S.; Paganin, D.M.; Siu, K.K.W. Quantitative single-exposure x-ray phase contrast imaging using a single attenuation grid. *Opt. Express* **2011**, *19*, 19781–19789. [CrossRef]
6. Weitkamp, T.; Diaz, A.; David, C.; Pfeiffer, F.; Stampanoni, M.; Cloetens, P.; Ziegler, E. X-ray phase imaging with a grating interferometer. *Opt. Express* **2005**, *13*, 6296–6304. [CrossRef]
7. Pavlov, K.M.; Li, H.; Paganin, D.M.; Berujon, S.; Rougé-Labriet, H.; Brun, E. Single-Shot X-Ray Speckle-Based Imaging of a Single-Material Object. *Phys. Rev. Appl.* **2020**, *13*, 054023. [CrossRef]
8. Morgan, K.S.; Paganin, D.M.; Siu, K.K.W. X-ray phase imaging with a paper analyzer. *Appl. Phys. Lett.* **2012**, *100*, 124102. [CrossRef]
9. Bérujon, S.; Ziegler, E.; Cerbino, R.; Peverini, L. Two-Dimensional X-Ray Beam Phase Sensing. *Phys. Rev. Lett.* **2012**, *108*, 158102. [CrossRef]
10. Gureyev, T.E.; Paganin, D.M.; Arhatari, B.; Taba, S.T.; Lewis, S.; Brennan, P.C.; Quiney, H.M. Dark-field signal extraction in propagation-based phase-contrast imaging. *Phys. Med. Biol.* **2020**, *65*, 215029. [CrossRef]
11. Stampanoni, M.; Mokso, R.; Marone, F.; Vila-Comamala, J.; Gorelick, S.; Trtik, P.; Jefimovs, K.; David, C. Phase-contrast tomography at the nanoscale using hard x rays. *Phys. Rev. B* **2010**, *81*, 140105. [CrossRef]
12. Donnelley, M.; Morgan, K.S.; Gradl, R.; Klein, M.; Hausermann, D.; Hall, C.; Maksimenko, A.; Parsons, D.W. Live-pig-airway surface imaging and whole-pig CT at the Australian Synchrotron Imaging and Medical Beamline. *J. Synchrotron Radiat.* **2019**, *26*, 175–183. [CrossRef] [PubMed]
13. Morgan, K.S.; Parsons, D.; Cmielewski, P.; McCarron, A.; Gradl, R.; Farrow, N.; Siu, K.; Takeuchi, A.; Suzuki, Y.; Uesugi, K.; et al. Methods for dynamic synchrotron X-ray respiratory imaging in live animals. *J. Synchrotron Radiat.* **2020**, *27*, 164–175. [CrossRef] [PubMed]
14. Mayo, S.C.; McCann, T.; Day, L.; Favaro, J.; Tuhumury, H.; Thompson, D.; Maksimenko, A. Rising dough and baking bread at the Australian synchrotron. *AIP Conf. Proc.* **2016**, *1696*, 020006. [CrossRef]
15. Khosravani, M.R.; Reinicke, T. On the Use of X-ray Computed Tomography in Assessment of 3D-Printed Components. *J. Nondestruct. Eval.* **2020**, *39*, 75. [CrossRef]
16. Sakellariou, A.; Arns, C.H.; Sheppard, A.P.; Sok, R.M.; Averdunk, H.; Limaye, A.; Jones, A.C.; Senden, T.J.; Knackstedt, M.A. Developing a virtual materials laboratory. *Mater. Today* **2007**, *10*, 44–51. [CrossRef]
17. Beltran, M.A.; Paganin, D.M.; Siu, K.K.W.; Fouras, A.; Hooper, S.B.; Reser, D.H.; Kitchen, M.J. Interface-specific x-ray phase retrieval tomography of complex biological organs. *Phys. Med. Biol.* **2011**, *56*, 7353. [CrossRef]
18. Arhatari, B.D.; De Carlo, F.; Peele, A.G. Direct quantitative tomographic reconstruction for weakly absorbing homogeneous phase objects. *Rev. Sci. Instrum.* **2007**, *78*, 053701. [CrossRef]
19. Gureyev, T.E.; Stevenson, A.W.; Paganin, D.; Mayo, S.C.; Pogany, A.; Gao, D.; Wilkins, S.W. Quantitative methods in phase-contrast X-ray imaging. *J. Digit. Imaging* **2000**, *13*, 121–126. [CrossRef]
20. Nesterets, Y.I.; Gureyev, T.E.; Mayo, S.C.; Stevenson, A.W.; Thompson, D.; Brown, J.M.; Kitchen, M.J.; Pavlov, K.M.; Lockie, D.; Brun, F.; et al. A feasibility study of X-ray phase-contrast mammographic tomography at the Imaging and Medical beamline of the Australian Synchrotron. *J. Synchrotron Radiat.* **2015**, *22*, 1509–1523. [CrossRef]
21. Radon, J. On the determination of functions from their integral values along certain manifolds. *IEEE Trans. Med. Imaging* **1986**, *5*, 170–176. [CrossRef]
22. Yokhana, V.S.K.; Arhatari, B.D.; Gureyev, T.E.; Abbey, B. Soft-tissue differentiation and bone densitometry via energy-discriminating X-ray microCT. *Opt. Express* **2017**, *25*, 29328–29341. [CrossRef]
23. Ingal, V.N.; Beliaevskaya, E.A.; Brianskaya, A.P.; Merkurieva, R.D. Phase mammography—A new technique for breast investigation. *Phys. Med. Biol.* **1998**, *43*, 2555–2567. [CrossRef]
24. Paganin, D.; Mayo, S.; Gureyev, T.E.; Miller, P.R.; Wilkins, S.W. Simultaneous phase and amplitude extraction from a single defocused image of a homogeneous object. *J. Microsc.* **2002**, *206*, 33–40. [CrossRef]
25. Nugent, K.A.; Gureyev, T.E.; Cookson, D.F.; Paganin, D.; Barnea, Z. Quantitative phase imaging using hard X rays. *Phys. Rev. Lett.* **1996**, *77*, 2961–2964. [CrossRef]
26. Koch, A.; Raven, C.; Spanne, P.; Snigirev, A. X-ray imaging with submicrometer resolution employing transparent luminescent screens. *J. Opt. Soc. Am. A* **1998**, *15*, 1940–1951. [CrossRef]
27. Insight Toolkit (ITK). Available online: https://itk.org/ (accessed on 5 December 2021).

28. McCormick, M.; Liu, X.; Ibanez, L.; Jomier, J.; Marion, C. ITK: Enabling reproducible research and open science. *Front. Neuroinform.* **2014**, *13*, 1–11. [CrossRef]

29. van Aarle, W.; Palenstijn, W.J.; Cant, J.; Janssens, E.; Bleichrodt, F.; Dabravolski, A.; De Beenhouwer, J.; Joost Batenburg, K.; Sijbers, J. Fast and flexible X-ray tomography using the ASTRA toolbox. *Opt. Express* **2016**, *24*, 25129–25147. [CrossRef]

30. Kak, A.C.; Slaney, M. *Principles of Computerized Tomographic Imaging*; IEEE Press: New York, NY, USA, 1988.

31. Marcou, J.; Bosworth, R.; Clarken, R.; Martin, P.; Moll, A. ASCI: A Compute platform for researchers at the Australian Synchrotron. In Proceedings of the 16th International Conference on Accelerator and Large Experimental Physics Control Systems (ICALEPCS 2017), Barcelona, Spain, 8–13 October 2017.

32. Nesterets, Y.I.; Gureyev, T.E. Noise propagation in x-ray phase-contrast imaging and computed tomography. *J. Phys. D Appl. Phys.* **2014**, *47*, 105402. [CrossRef]

33. Kitchen, M.J.; Buckley, G.A.; Gureyev, T.E.; Wallace, M.J.; Andres-Thio, N.; Uesugi, K.; Yagi, N.; Hooper, S.B. CT dose reduction factors in the thousands using X-ray phase contrast. *Sci. Rep.* **2017**, *7*, 15953. [CrossRef]